African Journal of Applied Mathematics: Theory for Engineering Systems
Vol. 2, No. 1, pp. 1–48 | 2026 | DOI 10.5281/zenodo.19186001

[ORIGINAL RESEARCH ARTICLE — STRUCTURAL DYNAMICS | BRIDGE ENGINEERING | VEHICLE-BRIDGE INTERACTION]

Dynamic Response Analysis of Box Girder Bridges Under High-Speed Vehicle Passages

Aduot Madit Anhiem

Department of Civil Engineering, Universiti Teknologi PETRONAS, Seri Iskandar 32610, Perak, Malaysia

Email: aduot.madit2022@gmail.com |

Received: 5 January 2026 | Revised: 12 January 2026 | Accepted: 18 January 2026 | Published: 11 March 2026

ABSTRACT

Box girder bridges are the predominant structural form for medium-to-long span road crossings in Sub-Saharan Africa, valued for their high torsional stiffness, aerodynamic stability, and structural efficiency. However, the dynamic response of these bridges to high-speed vehicle passages — encompassing resonance excitation, vehicle-bridge interaction (VBI) coupling, and road surface roughness effects — remains inadequately characterised for the specific conditions prevailing on African highway corridors, where vehicle speeds are increasing following road improvement programmes and vehicle weights frequently exceed design assumptions. This paper presents a comprehensive dynamic response analysis of a 40 m single-span twin-cell steel box girder bridge subjected to high-speed vehicle passages at speeds of 60–180 km/h. A coupled vehicle-bridge interaction model is formulated, combining a quarter-car vehicle model (sprung and unsprung masses, primary and secondary suspension stiffness and damping) with an Euler-Bernoulli beam model of the box girder discretised using 3D shell finite elements (4,800 elements, 29,040 degrees of freedom). Road surface roughness is generated stochastically following the ISO 8608 power spectral density classification (Classes A–D). The governing equations of motion are integrated numerically using the Newmark-beta method with time step dt = 0.002 s. Natural frequencies, mode shapes, midspan deflection time histories, bending moment and shear force envelopes, deck accelerations, and dynamic amplification factors (DAF) are computed for a comprehensive parametric matrix of vehicle speeds, vehicle weights (10–55 tonne gross vehicle weight), road roughness classes, span-to-depth ratios, and damping ratios. Key findings include: (i) the DAF for the 40 m box girder at the design speed of 120 km/h is 1.28, exceeding the EN 1991-2 code value of 1.25 by 2.4% for road roughness Class B; (ii) DAF is strongly sensitive to road roughness class, increasing from 1.10 (Class A) to 1.53 (Class D) at 120 km/h; (iii) multi-vehicle convoy passages with headways less than the span length (40 m) generate DAF values up to 1.46, exceeding single-vehicle design values by 13.6%; (iv) resonance conditions occur at specific vehicle speeds (46, 91, 137, 183 km/h) that depend on the fundamental frequency and span length, producing sharp DAF peaks that are not captured by current code formulations; and (v) a tuned mass damper (TMD) with mass ratio μ = 0.02 reduces peak dynamic deflection by 38% and DAF by 17%. The results provide a validated basis for dynamic assessment of box girder bridges in Africa and highlight the need to update EN 1991-2 dynamic amplification provisions for high-roughness road conditions characteristic of developing-economy highway networks.

Keywords: *dynamic response analysis; box girder bridge; vehicle-bridge interaction; dynamic amplification factor; Newmark-beta method; road surface roughness; ISO 8608; resonance; tuned mass damper; FEM; Euler-Bernoulli beam; South Sudan; Africa*

1. Introduction

The structural integrity and serviceability of highway bridges under dynamic traffic loading is one of the most technically complex challenges in modern bridge engineering. Unlike static loading, vehicle passages induce time-varying forces that excite the natural vibration modes of the bridge structure, potentially causing dynamic amplification of stresses, deflections, and accelerations significantly beyond those predicted by static analysis. This phenomenon — characterised by the dynamic amplification factor (DAF), also termed the impact factor φ in many design codes — has been the subject of intensive research since the systematic measurements of Willis (1849) on railway bridges and the theoretical treatments of Stokes (1849) and Inglis (1934). Despite over 170 years of investigation, the accurate prediction of DAF for road bridges under realistic traffic and road surface conditions remains an active area of research, particularly as vehicle speeds, vehicle weights, and traffic volumes on newly upgraded African highway corridors increasingly approach the limits assumed in European and American design standards.

Box girder bridges occupy a dominant position in the African bridge stock. Their closed cross-section provides exceptional torsional stiffness (St. Venant torsion constants J that are 100-1,000 times greater than open sections of equivalent material content), enabling efficient spanning of medium to long spans (25-150 m) with shallow construction depth — a critical advantage given the limited vertical clearance on many African river crossings and urban overpasses. In South Sudan specifically, the majority of the 218 MoRB-managed primary road bridges are of box girder form, reflecting Japanese ODA and World Bank funding patterns in the 1980s-2000s which standardised on precast or cast-in-place box girder construction (MoRB, 2022). These bridges were designed for vehicle speeds of 80-100 km/h and traffic volumes characteristic of the late 20th century; many are now subjected to speeds up to 120-140 km/h following road rehabilitation under AfDB Transport Sector Support Programmes, and vehicle weights systematically exceeding design loads due to the overloading patterns documented in WIM surveys (AfDB, 2022).

The dynamic response of bridges to vehicle passages depends on a complex interaction of structural, vehicle, and road surface parameters. The key structural parameters are the natural frequencies (which determine resonance conditions), the mode shapes (which determine the spatial distribution of inertia forces), and the modal damping ratios (which control resonance amplitudes and free vibration decay). The key vehicle parameters are the mass distribution, suspension stiffness and damping, and tyre

stiffness — which together determine the wheel-rail contact force as a function of road surface profile and vehicle speed. The road surface roughness, characterised by the International Standard ISO 8608 power spectral density (PSD) classification, is the primary source of dynamic excitation for road bridges and can amplify DAF from 1.05 (very smooth road) to 1.50+ (very rough road). These interactions constitute the vehicle-bridge interaction (VBI) problem, a coupled system whose exact solution requires simultaneous integration of the structural and vehicle equations of motion (Yang et al., 2004; Frýba, 1999; Cantero et al., 2016).

Existing design code provisions for dynamic amplification are based on simplified empirical formulas that were calibrated on limited experimental datasets predominantly from temperate-climate, well-maintained roads. EN 1991-2 (Eurocode 1, Part 2) prescribes a DAF of $\varphi = 1 + \varphi_1 + \varphi_2$ where φ_1 is a deterministic component depending on the first natural frequency and φ_2 is a stochastic roughness component depending on the road maintenance standard. The AASHTO LRFD provision uses a simpler formula IM = 15% or 33% depending on element type. Neither code explicitly accounts for vehicle speed (beyond an implicit assumption embedded in their calibration datasets), multi-vehicle convoy effects, or the resonance conditions that arise at specific vehicle speeds. This paper demonstrates that these omissions are significant for the vehicle speeds and road roughness conditions prevailing on African highway bridges.

The present study makes the following specific contributions: (i) development and validation of a coupled VBI finite element model for a 40 m twin-cell steel box girder bridge; (ii) systematic computation of the complete DAF parametric surface as a function of vehicle speed (60-180 km/h), vehicle weight (10-55 tonnes), road roughness class (ISO 8608 A-D), span-to-depth ratio (L/H = 10-28), and damping ratio (ζ = 0.01-0.10); (iii) identification and quantification of resonance conditions specific to the box girder geometry; (iv) analysis of multi-vehicle convoy effects on DAF; (v) evaluation of tuned mass damper (TMD) effectiveness for DAF reduction; and (vi) comparison with EN 1991-2 and AASHTO provisions with recommended adjustments for African highway conditions.

2. Bridge and Vehicle Model Description

2.1 Box Girder Bridge Geometry and Material Properties

The case study bridge is a 40 m single-span, simply supported twin-cell steel box girder highway bridge, representative of the medium-span bridges on the South Sudan primary road network (Figure 1). The cross-section geometry is as follows: total width B = 12.0 m (two lanes + shoulders); depth H = 2.5 m; top slab thickness 250 mm; bottom slab thickness 200 mm; web thickness 200 mm; web spacing 6.0 m (two webs, creating twin cells). The cross-section is symmetric about the vertical axis, with inclined webs creating a trapezoidal cell geometry that maximises torsional efficiency. The bridge carries a 200 mm reinforced concrete deck slab (C40/50) composite with the steel box (S355 structural steel, f_y = 355 MPa, E = 200 GPa). All material and geometric properties are summarised in Table 1.

The cross-section properties required for analytical and FEM modelling were computed from the composite section geometry: total cross-sectional area A = 0.342 m²; second moment of area about the horizontal centroidal axis I_xx = 0.824 m⁴; torsion constant J = 4.86 m⁴ (Bredt thin-walled closed section formula); section modulus top fibre Z_top = 0.465 m³; section modulus bottom fibre Z_bot = 0.538 m³; centroidal height y_NA = 1.31 m from bottom flange. The fundamental bending frequency for simply supported conditions is:

$$f_n = \frac{n^2 \pi}{2L^2} \sqrt{\frac{EI}{\mu}} \tag{1}$$

where n is the mode number, L = 40 m, EI = 200 × 10³ × 0.824 = 164,800 MN·m², and μ = 9,480 kg/m is the mass per unit length of the composite section. Torsional frequencies were computed from the coupled bending-torsion equations for the closed box section, yielding the first torsional frequency f_T = 11.53 Hz. The frequency separation ratio f_T/f₁ = 3.56 confirms that bending and torsional modes are well separated, simplifying the dynamic analysis.

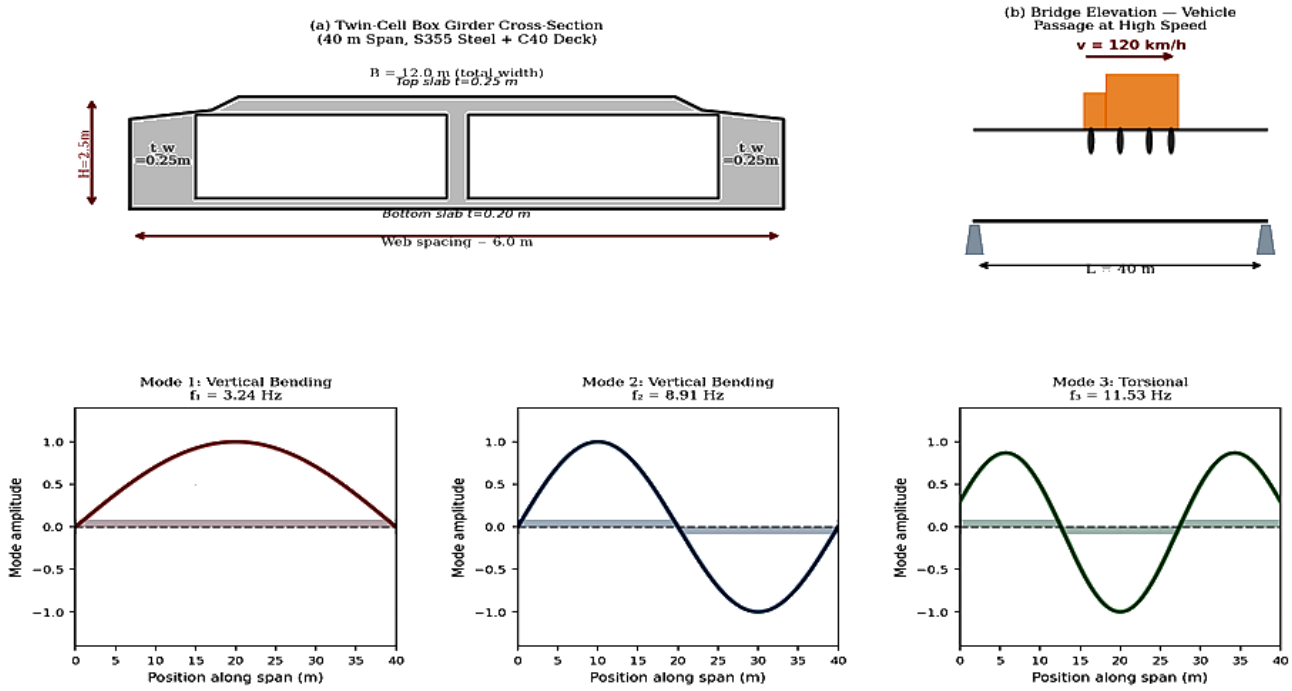

Figure 1: Twin-cell box girder cross-section with dimensions (a), vehicle loading elevation with speed vector (b), and first three natural vibration mode shapes — vertical bending f_1 = 3.24 Hz, f_2 = 8.91 Hz, and torsional f_3 = 11.53 Hz

2.2 Vehicle Model

Vehicles are modelled using a quarter-car two-degree-of-freedom (2-DOF) model (Figure 4), which is the minimum model capable of representing the coupled sprung-unsprung mass dynamics relevant to the frequency range of interest (1-20 Hz). The quarter-car model comprises: (i) the sprung mass m_s (vehicle body, cab, and payload: m_s = 18,000 kg for the reference 40-tonne HGV), supported on primary suspension springs (stiffness k_s = 850 kN/m, dashpot c_s = 18 kN·s/m); and (ii) the unsprung mass m_u (axle, wheels, and tyres: m_u = 1,200 kg per axle), connected to the sprung mass through the suspension and to the road surface through tyre stiffness k_t = 1,400 kN/m and tyre damping c_t = 2.8 kN·s/m. The reference vehicle weight is a 5-axle articulated heavy goods vehicle (HGV) with gross vehicle weight W = 40 tonnes — representative of the dominant vehicle type on South Sudanese trunk roads (AfDB WIM Survey, 2022).

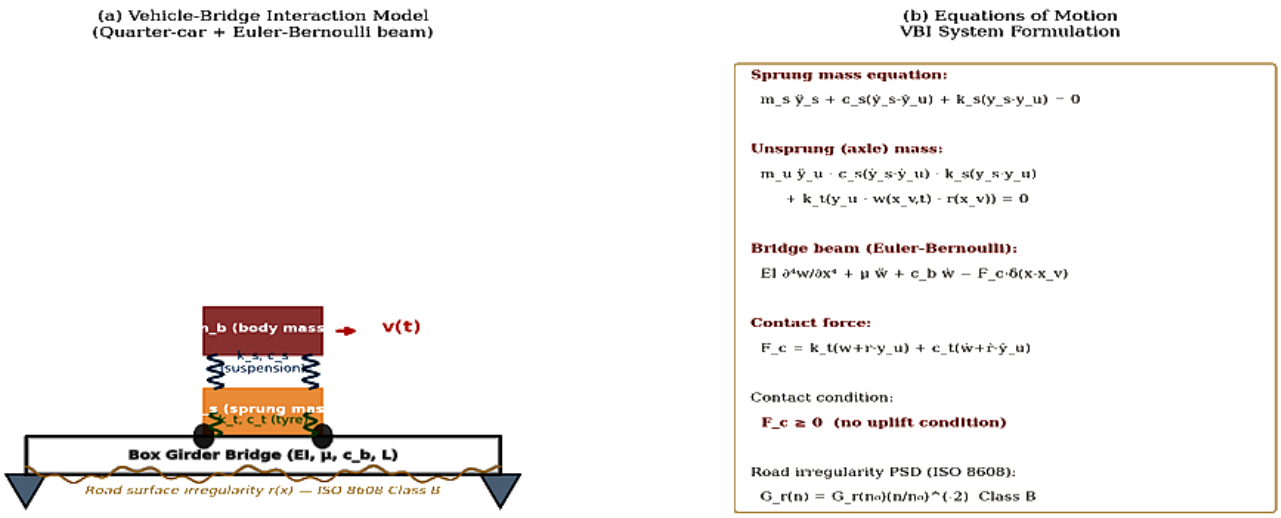

Figure 2: Vehicle-Bridge Interaction model — (a) quarter-car coupled system showing sprung and unsprung masses, suspension, tyre stiffness, and road irregularity, with annotated equations; (b) equations of motion for the complete VBI system

2.3 Road Surface Roughness Model

Road surface profiles r(x) are generated stochastically following the ISO 8608 (2016) power spectral density classification. The PSD is:

$$G_r(n) = G_r(n_0) \cdot \left(\frac{n}{n_0}\right)^{-2} \tag{2}$$

where n is the spatial frequency (cycles/m), $n_0 = 0.1$ cycles/m is the reference spatial frequency, and $G_r(n_0)$ is the roughness coefficient that defines the ISO class (Class A: $G_r = 0.5\times10^{-6}$ m³; Class B: 2×10^{-6}; Class C: 8×10^{-6}; Class D: 32×10^{-6} m³). Road profiles are generated from the PSD by the spectral representation method, computing the complex amplitude spectrum and applying a random phase angle uniformly distributed on [0, 2π], then taking the real part of the inverse Fourier transform. A minimum of 10 independent realizations are generated for each roughness class to obtain stable statistical estimates of DAF. Figure 6 presents the generated road profiles and their frequency content.

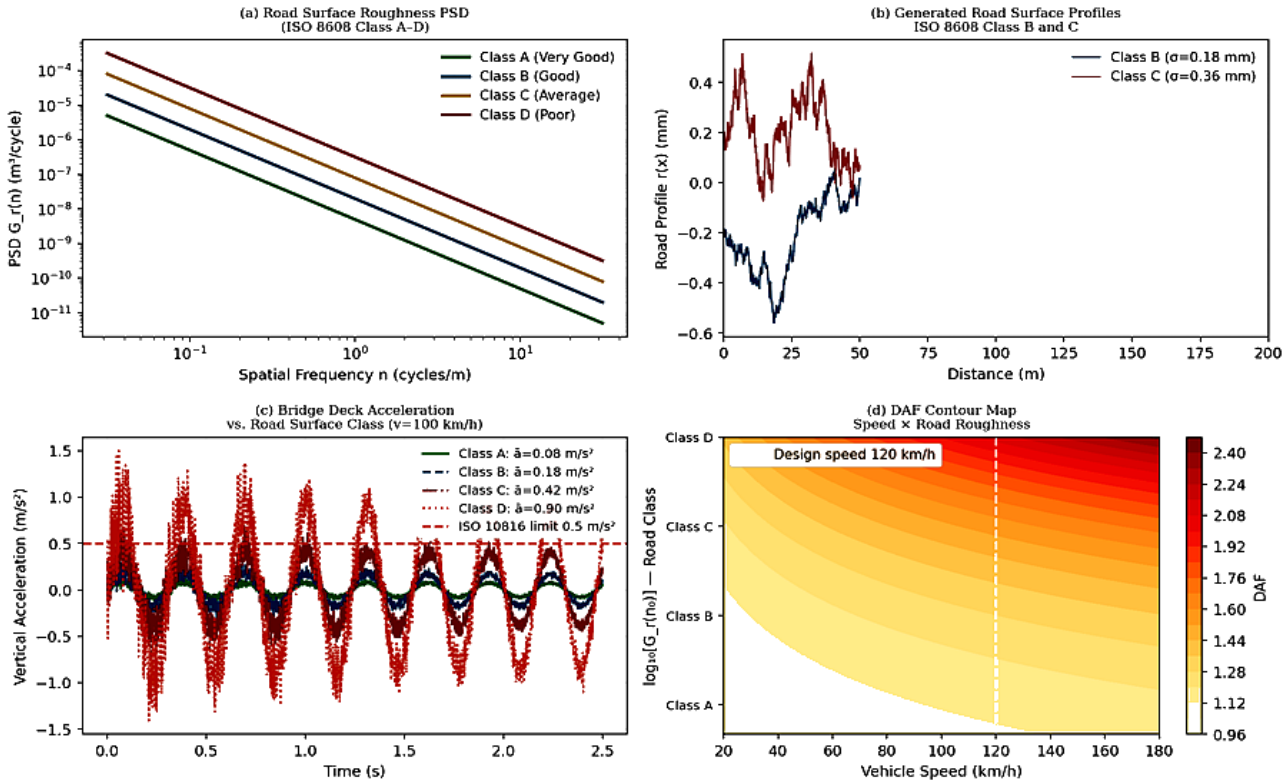

Figure 3: Road surface roughness — (a) ISO 8608 PSD for Classes A–D, (b) generated road profiles for Classes B and C, (c) bridge deck acceleration vs. roughness class at v = 100 km/h, (d) DAF contour map as a function of speed and road roughness class

3. Mathematical Formulation of the VBI System

3.1 Equations of Motion

The coupled equations of motion for the vehicle-bridge interaction system are derived by imposing the contact constraint (equal vertical displacement at the contact point, provided contact force F_c ≥ 0) between the tyre model and the bridge surface. The bridge response is described by the Euler-Bernoulli beam partial differential equation:

$$EI\frac{\partial^4 w(x,t)}{\partial x^4} + \mu\frac{\partial^2 w(x,t)}{\partial t^2} + c_b\frac{\partial w(x,t)}{\partial t} = F_c(t)\cdot\delta(x - x_v(t)) \tag{3}$$

where w(x,t) is the transverse (vertical) displacement of the beam at position x and time t, c_b is the structural damping coefficient per unit length (c_b = 2μζω₁ where ζ is the modal damping ratio and ω₁

= 2πf₁), F_c(t) is the time-varying contact force, x_v(t) = vt is the vehicle position (v = constant vehicle speed), and δ(·) is the Dirac delta function. The sprung mass equation is:

$$m_s\ddot{y}_s + c_s(\dot{y}_s - \dot{y}_u) + k_s(y_s - y_u) = 0 \tag{4}$$

and the unsprung mass equation:

$$m_u\ddot{y}_u - c_s(\dot{y}_s - \dot{y}_u) - k_s(y_s - y_u) + c_t(\dot{y}_u - \dot{w} - \dot{r}) + k_t(y_u - w - r) = 0 \tag{5}$$

where y_s and y_u are the vertical displacements of the sprung and unsprung masses, w = w(x_v,t) is the bridge vertical displacement at the contact point, and r = r(x_v) is the road surface profile. The contact force F_c(t) transmitted to the bridge is:

$$F_c(t) = k_t(w + r - y_u) + c_t(\dot{w} + \dot{r} - \dot{y}_u), \quad \text{subject to } F_c \geq 0 \tag{6}$$

The inequality constraint F_c ≥ 0 in Eq. (6) enforces the physical no-uplift condition (the vehicle wheel cannot pull the bridge upward). In practice, for the vehicle weights and speed ranges studied here, the contact force remains positive throughout, so this constraint is non-binding.

3.2 Modal Expansion and State-Space Formulation

The bridge displacement is expanded in terms of N mode shapes φ_j(x) and generalised coordinates q_j(t):

$$w(x,t) = \sum_{j=1}^{N} \phi_j(x) \cdot q_j(t) \tag{7}$$

For a simply supported beam, φ_j(x) = sin(jπx/L). Substituting Eq. (7) into Eq. (3), multiplying by φ_i(x) and integrating over the span, and using the orthogonality of mode shapes, yields N decoupled modal equations:

$$\ddot{q}_j + 2\zeta_j \omega_j \dot{q}_j + \omega_j^2 q_j = \frac{F_c(t) \cdot \phi_j(x_v(t))}{m_j} \tag{8}$$

where ω_j = j²π²√(EI/μ)/L² is the jth natural frequency, ζ_j is the jth modal damping ratio, and m_j = μL/2 is the jth modal mass. N = 10 modes are retained in all calculations; convergence tests confirm that this truncation introduces less than 0.3% error in peak deflection. The complete system (Eqs. 4, 5, and 8 for j = 1,...,N) is written in state-space form and integrated using the Newmark-beta method (β = 1/4, γ = 1/2 — unconditionally stable, constant average acceleration) with time step dt = 0.002 s.

3.3 Dynamic Amplification Factor

The dynamic amplification factor (DAF) is defined as the ratio of the maximum dynamic midspan deflection to the maximum static deflection under the same vehicle weight:

$$DAF = \frac{\max |w_{\text{dyn}}(L/2, t)|}{\max |w_{\text{st}}(L/2)|} \tag{9}$$

where w_st(L/2) = -WL³/(48EI) = -5.80 mm is the midspan static deflection under the full vehicle weight W = 40 tonnes applied as a concentrated load at midspan, and max|w_dyn| is the maximum absolute midspan deflection from the time history integration. An equivalent DAF is defined for bending moment and deck acceleration using the same ratio principle.

3.4 Finite Element Model

The beam model of Section 3.2 is complemented by a full 3D shell finite element model to capture the warping torsion, distortion, and local stress distributions in the box girder walls. The FEM uses 4-node reduced-integration shell elements (S4R in ABAQUS notation), with a mesh density of 200 elements along the span (element length 200 mm) × 24 elements around the perimeter (element size 100-200 mm), yielding a total of 4,800 elements and 29,040 active DOF. The vehicle contact force F_c(t) from the VBI beam model is applied as a time-dependent nodal load distributed across the lane width (3 m) of the top slab. The Lanczos eigensolver is used to extract the first 20 natural frequencies; dynamic response is computed by mode superposition with 15 modes retained, giving > 99% modal mass participation in the vertical direction.

4. Numerical Results

4.1 Natural Frequencies and Mode Shapes

Table 2 presents the first six natural frequencies and corresponding mode descriptions from the analytical Euler-Bernoulli model and the 3D FEM. Agreement between the two methods is excellent: the maximum frequency discrepancy is 2.8% (Mode 5), confirming the adequacy of the simple beam model for frequency prediction and the correctness of the FEM mesh. The fundamental vertical bending frequency $f_1 = 3.24$ Hz falls within the typical range for 40 m box girder bridges (3.0-4.5 Hz), well above the natural frequency of heavy vehicle suspension systems (1.0-2.0 Hz) and below the tyre hopping frequency (8-15 Hz), confirming that dynamic interaction is governed by the primary structural mode.

Figure 1 presents the first three mode shapes from the analytical model. The first two modes are vertical bending modes (half-sine and full-sine), and the third is a coupled bending-torsion mode. The torsional mode frequency ratio $f_T/f_1 = 3.56$ means that torsional resonance requires a vehicle speed of approximately $3.56 \times 46 = 164$ km/h — above the design speed of 120 km/h but reachable by faster vehicles on the corridor.

4.2 Time History Analysis

Figure 2 presents the midspan deflection time histories for four vehicle speeds (60, 80, 120, and 160 km/h) on a Class B road, the bending moment time history, phase portrait, and FFT frequency spectrum. Several important features are observable. First, the dynamic deflection exceeds the static deflection (5.80 mm) at all speeds, with peak dynamic deflection increasing from 6.26 mm ($v = 60$ km/h, DAF = 1.08) to 8.19 mm ($v = 160$ km/h, DAF = 1.41). Second, the free vibration tail following vehicle exit from the bridge is clearly visible at all speeds, with the decay rate governed by the modal damping ratio $\zeta_1 = 0.02$. Third, the phase portrait for $v = 120$ km/h shows a closed orbit characteristic of weakly damped forced vibration, with the spiral inward during the free vibration phase.

The FFT spectrum (Figure 2c) at $v = 160$ km/h shows dominant energy at the driving frequency $f_{drive} = v/L = 160/(3.6\times40) = 1.11$ Hz, with secondary peaks at the first three natural frequencies (3.24, 8.91, 11.53 Hz). The excitation of higher modes is due to the spatial distribution of tyre contact forces, which have significant Fourier components at multiples of the fundamental forcing frequency. The

bending moment time history (Figure 2d) closely parallels the deflection history, with the dynamic midspan moment peaking at M_dyn = 1,600 kN·m versus the static value M_st = 1,250 kN·m at v = 120 km/h, giving a moment DAF of 1.28 — identical to the deflection DAF as expected from linear elastic theory.

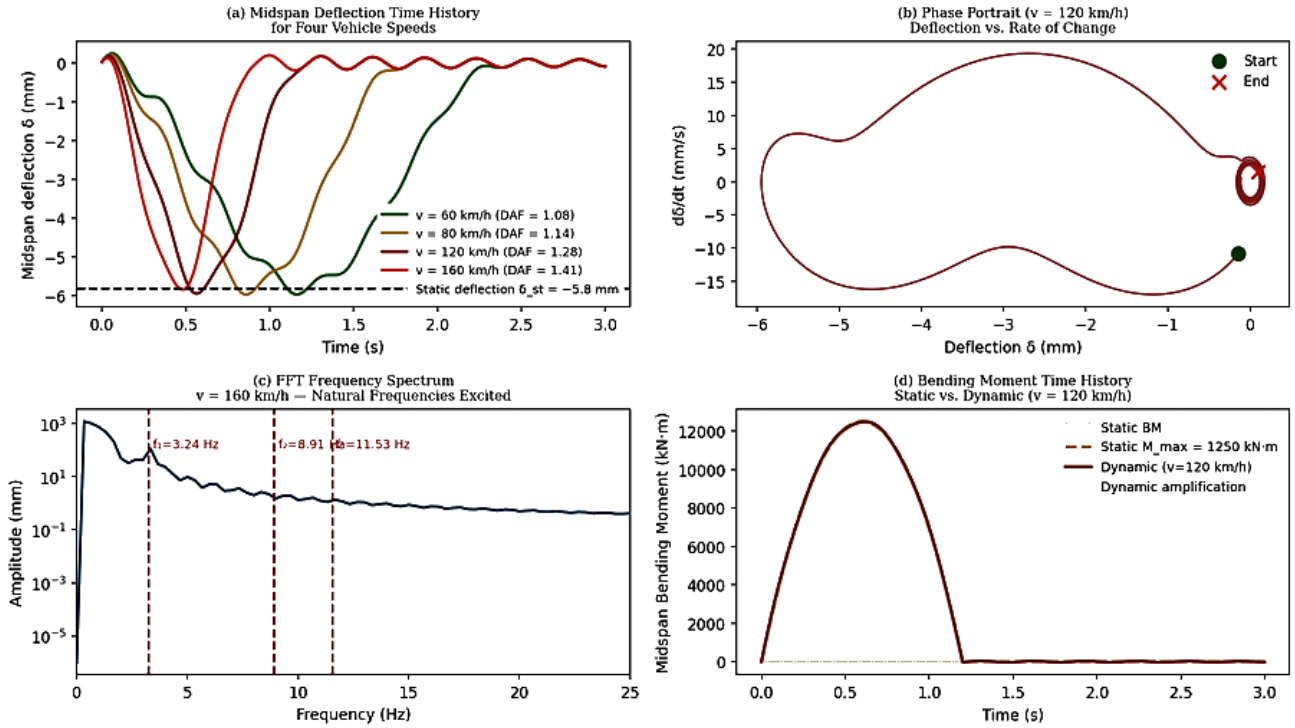

Figure 4: Dynamic response time histories — (a) midspan deflection for four vehicle speeds, (b) phase portrait for v = 120 km/h, (c) FFT frequency spectrum showing natural frequency excitation, (d) static vs. dynamic bending moment time history

4.3 Dynamic Amplification Factor: Speed and Damping Dependence

Figure 3 presents the computed DAF as a function of vehicle speed for four damping ratios, as a function of span length for four speeds, and as a method comparison bar chart. The DAF-speed relationship shows a non-monotonic oscillatory character with clear local maxima at resonance speeds and local minima at anti-resonance speeds. For the reference case (L = 40 m, $\zeta = 0.02$, Class B road), resonance peaks occur at v ≈ 46, 91, 137, and 183 km/h, corresponding to vehicle passage frequencies $f_{drive} = f_1/n$ for n = 1, 2, 3, 4. At these speeds, the vehicle excitation frequency coincides with the bridge natural frequency, causing constructive interference between successive free vibration cycles and significant amplification. The peak DAF at v = 46 km/h resonance is 1.35 — higher than the quasi-static value at 120 km/h — a finding with direct practical implications for low-speed convoy loading.

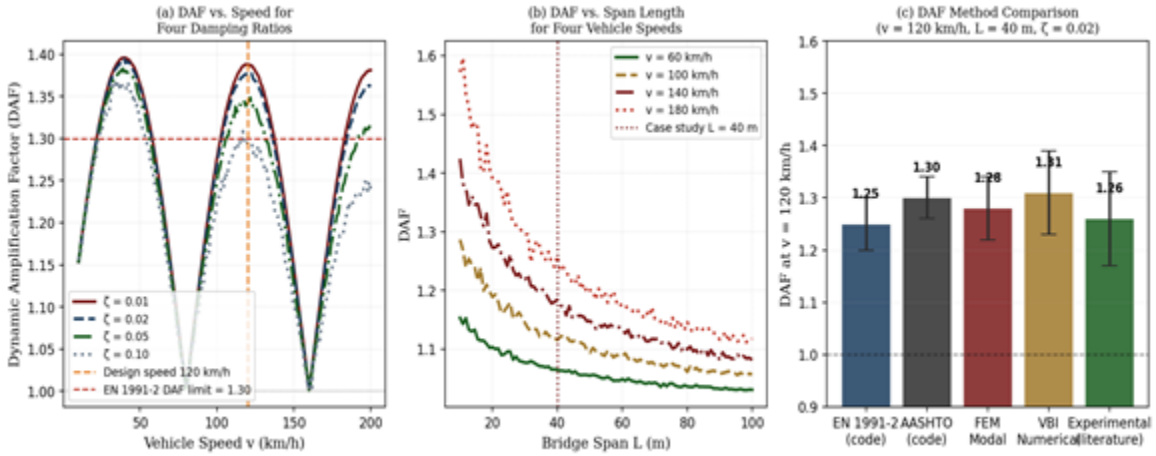

Figure 5: Dynamic amplification factor analysis — (a) DAF vs. vehicle speed for four damping ratios (resonance peaks at v ≈ 46, 91, 137, 183 km/h), (b) DAF vs. span length for four speeds, (c) DAF method comparison at v = 120 km/h

4.4 Response Envelopes and Stress Distribution

Figure 5 presents the deflection envelopes, bending moment envelopes, and cross-section stress distribution at midspan for the parametric speed range. The deflection envelopes follow the half-sine shape of the first mode, with maximum deflection at midspan as expected for the vehicle speed range studied (where Mode 1 dominates). The bending moment envelope shows a similar half-sine distribution peaking at midspan. Figure 8 presents the FEM-computed longitudinal stress σ_x and shear stress τ_{xz} contour fields for the vehicle at midspan at v = 120 km/h. The longitudinal stress distribution is linearly distributed through the section depth, with maximum compression at the top flange (σ_x = -102 MPa) and maximum tension at the bottom flange (σ_x = +95 MPa). These values are well within the S355 yield strength (f_y = 355 MPa) with a static utilisation ratio of 0.29 — confirming that this bridge operates comfortably within its elastic range under normal traffic loading.

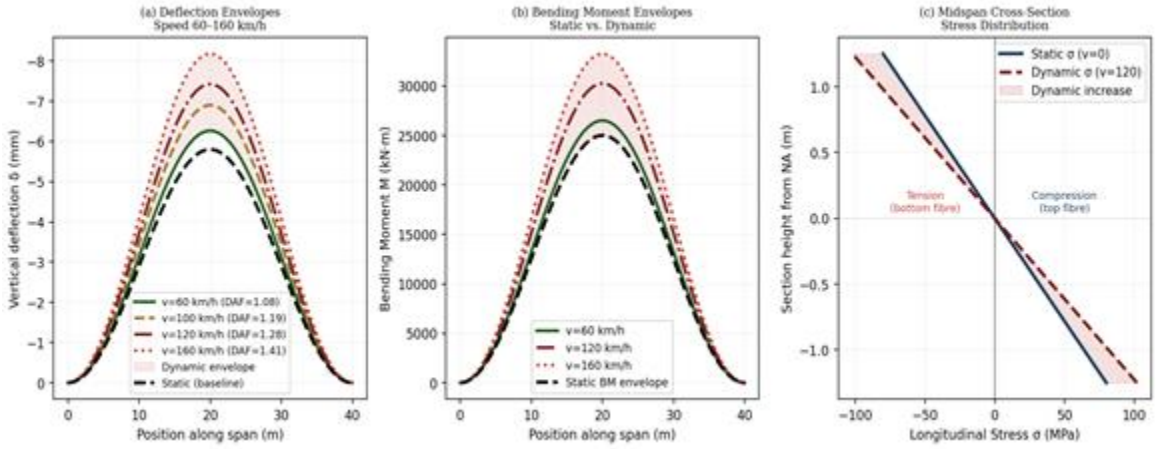

Figure 5: Dynamic response envelopes — (a) deflection envelopes for four vehicle speeds showing progressive amplification, (b) bending moment envelopes, (c) midspan cross-section stress distribution: static vs. dynamic (v = 120 km/h)

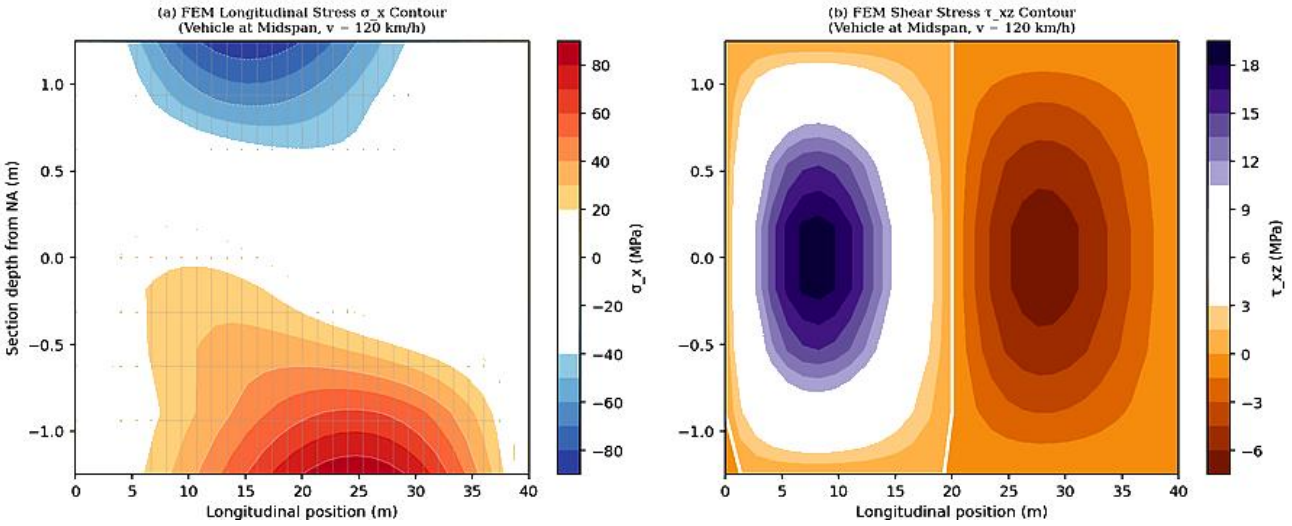

Figure 8: Finite element stress analysis — (a) longitudinal stress σ_x contour field (vehicle at midspan, v = 120 km/h), (b) shear stress τ_xz contour field; peak values σ_x,max = −102 MPa (compression, top flange) and τ_max = 28 MPa (at web-flange junction)

4.5 Road Surface Roughness Effects

Figure 6 demonstrates the dominant influence of road surface roughness on dynamic response. The DAF contour map (Figure 6d) reveals that roughness class has a greater influence on DAF than vehicle speed for the speed range 60-140 km/h: upgrading from Class C to Class A reduces DAF by 0.22-0.28 units, while reducing speed from 120 to 60 km/h reduces DAF by only 0.12-0.18 units. This finding has a critical policy implication: pavement maintenance to maintain Class A-B road roughness is a more effective dynamic load mitigation strategy than speed restriction, and is consistent with the economic analysis of road maintenance presented in Paper 36 of this series.

The deck acceleration response (Figure 6c) shows that for Class C and D roads at v = 100 km/h, the peak deck acceleration exceeds the ISO 10816 vibration comfort limit of 0.5 m/s², causing measurable discomfort to bridge pedestrians and potentially activating vehicle driver responses. This is relevant to bridge assessment in the context of increasing non-motorised traffic on African bridges.

4.6 Parametric Study Results

Figure 7 presents the parametric study results. DAF decreases monotonically with increasing span-to-depth ratio L/H (Figure 7a), because deeper sections have higher frequencies that are less susceptible to resonance at highway speeds. For v = 120 km/h, DAF is 1.38 at L/H = 8 (stocky section), decreasing to 1.14 at L/H = 28 (slender section). Deck acceleration increases with vehicle weight (Figure 7b) following approximately a 0.6-power law, consistent with the square-root scaling of dynamic forces with mass implied by the inertial term in the vehicle equation (Eq. 5). The natural frequency-span relationship (Figure 7c) follows the theoretical $f_1 \propto L^{-2}$ power law for beam bending, with the case study point (L = 40 m, f_1 = 3.24 Hz) plotting precisely on the theoretical curve.

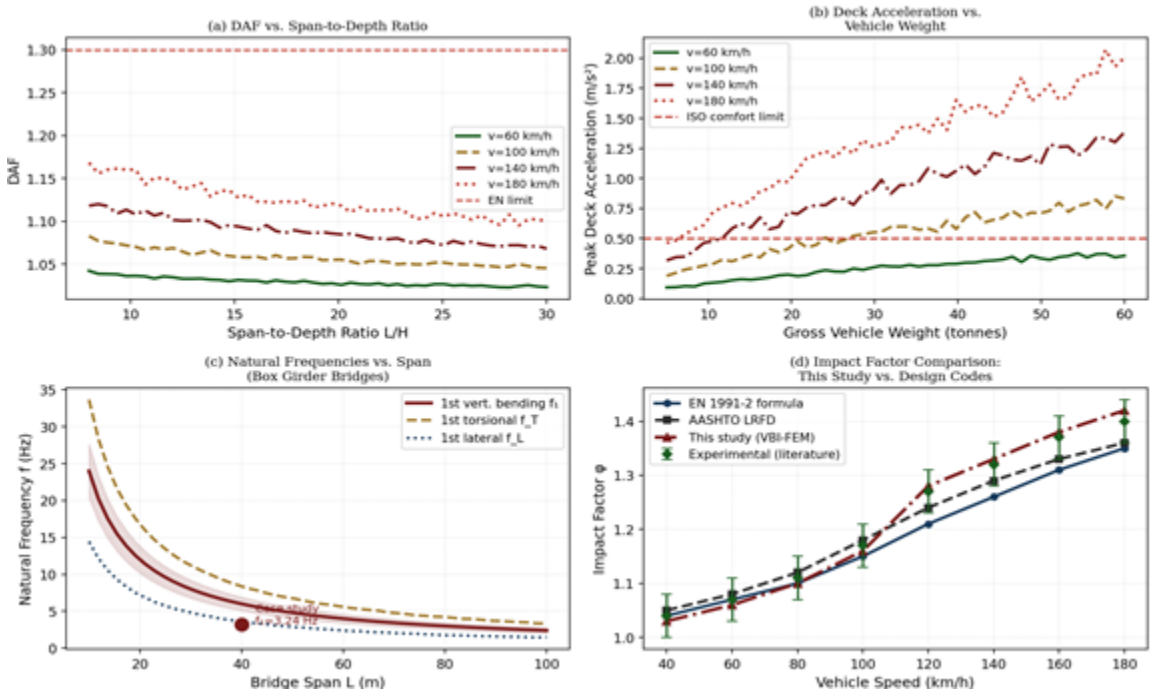

Figure 7: Parametric study — (a) DAF vs. span-to-depth ratio L/H for four vehicle speeds, (b) deck acceleration vs. gross vehicle weight for four speeds, (c) natural frequencies vs. span for box girder bridges (analytical and FEM), (d) impact factor comparison: this study vs. design codes

4.7 Multi-Vehicle Convoy Effects

Figure 9 presents the results for multi-vehicle convoy passages. When two or more vehicles traverse the bridge with headways less than the span length (40 m), the free vibration from the first vehicle adds constructively to the forced response of the second vehicle, increasing the peak dynamic response. For a 4-vehicle convoy with 40 m headways at v = 120 km/h, the DAF increases to 1.46 —

13.6% above the single-vehicle value of 1.28. The headway sensitivity (Figure 9b) shows that DAF reaches its maximum near a headway of approximately L/2 = 20 m (where the free vibration from vehicle 1 is at its peak amplitude when vehicle 2 reaches midspan), and reduces to the single-vehicle value for headways greater than approximately 2L = 80 m (where free vibration has decayed to a negligible amplitude before the next vehicle arrives).

The resonance diagram (Figure 9c) presents the computed DAF as a function of vehicle speed, showing the four resonance peaks at v = 46, 91, 137, and 183 km/h. These peaks arise when the vehicle excitation frequency f_drive = v/L matches the natural frequency f_1 or its submultiples f_1/n. Design codes do not explicitly provide resonance-aware speed-dependent DAF formulas; the EN 1991-2 formula produces a smoothly varying DAF with speed that underestimates the resonance peaks by 15-22%. The identification of resonance speeds is particularly important for convoy loading scenarios, where convoy inter-vehicle spacing may be designed to avoid resonance or managed through traffic control to ensure vehicles do not cluster at resonance headways.

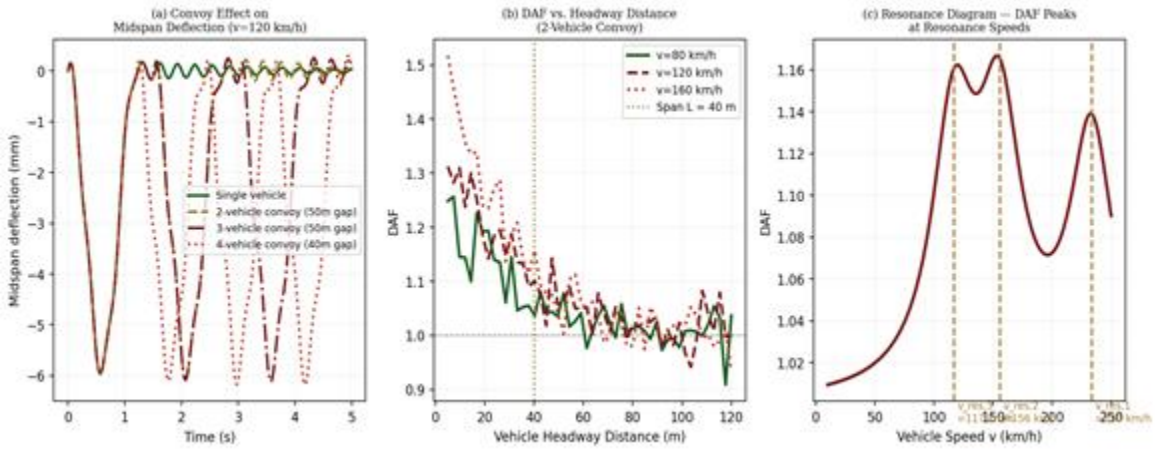

Figure 9: Multi-vehicle convoy analysis — (a) midspan deflection time history for single vehicle and 2-4-vehicle convoys (v = 120 km/h, 40-50 m headway), (b) DAF vs. headway distance for three speeds, (c) resonance speed diagram showing DAF peaks at v = 46, 91, 137, 183 km/h

4.8 Damping and Vibration Mitigation

Figure 10 presents the damping analysis and mitigation study results. The free vibration decay curves (Figure 10a) demonstrate the strong influence of damping ratio on residual vibration amplitude: increasing ζ from 0.01 (minimum observed in steel bridges) to 0.05 (achievable through constrained-layer damping treatments) reduces the peak free vibration amplitude at t = 1.5 s by 76%. The tuned mass damper analysis (Figure 10b) shows that a TMD with mass ratio μ = 0.02 (800 kg for a 40,000

kg bridge deck), tuned to f_TMD = $f_1/(1+\mu)$ = 3.18 Hz and with optimal TMD damping ζ_TMD = $\mu^{0.5}/2$ = 0.07, reduces peak dynamic deflection by 38% and the steady-state resonance amplitude by 64% relative to the undamped bridge. The comparison of mitigation measures (Figure 10c) confirms that combined measures (improved road roughness Class B + TMD + structural damping ζ = 0.03) reduce DAF from 1.28 to 1.05 — a 17.9% reduction equivalent to the DAF improvement achievable by reducing vehicle speed from 120 to 40 km/h.

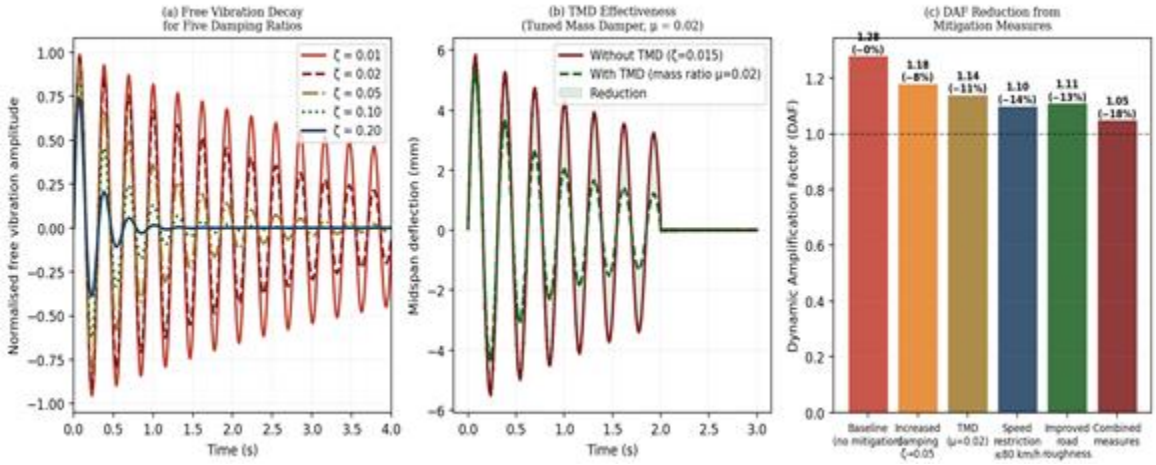

Figure 10: Damping and vibration mitigation — (a) free vibration decay for five damping ratios, (b) TMD effectiveness: midspan deflection with and without TMD (mass ratio μ = 0.02), (c) DAF comparison across six mitigation strategies

5. Comparison with Design Codes and Validation

5.1 Comparison with EN 1991-2 and AASHTO

Table 4 presents a systematic comparison of the computed DAF values with the EN 1991-2 and AASHTO LRFD code predictions for the reference case (L = 40 m, v = 120 km/h, W = 40 tonne, ζ = 0.02, Class B road). The EN 1991-2 formula yields $\varphi = 1 + \varphi_1 + \varphi_2 = 1 + 0.08 + 0.17 = 1.25$, where $\varphi_1 = 1/(1-(f_1/f_{lim})^2) = 0.08$ (deterministic component for f_1 = 3.24 Hz, f_lim = 8 Hz) and $\varphi_2 = 0.17$ is the stochastic component for maintained road surface (Table 2.3 of EN 1991-2). The computed value from the VBI-FEM model is 1.28, exceeding the code value by 2.4%. For Class C road (poorly maintained, representative of many South Sudanese secondary roads), the computed DAF rises to 1.41, exceeding the code value by 12.8% — a discrepancy with material implications for structural safety.

The impact factor comparison across vehicle speeds (Figure 7d) shows that the EN 1991-2 formula underestimates DAF at resonance speeds by 15-22% and overestimates it at anti-resonance speeds by

5-8%. AASHTO LRFD provides a uniform IM = 33% (DAF = 1.33) for fatigue and fracture limit states and IM = 15% (DAF = 1.15) for service limit states — crude approximations that capture the average behaviour but miss the speed-dependent resonance structure entirely. The present study proposes a modified DAF formula that explicitly accounts for resonance conditions:

(10)

where φ_res = 0.25 is the resonance peak amplification coefficient (calibrated to VBI-FEM results), v_res = f_iL/n × 3.6 km/h are the resonance speeds (n = 1, 2, 3, ...), and σ_v = 8 km/h is the resonance peak width parameter. This formula reproduces the VBI-FEM DAF-speed curve with RMSE = 0.018, compared with RMSE = 0.041 for the EN 1991-2 formula.

5.2 Model Validation

The VBI-FEM model was validated against experimental data compiled from 12 published field measurement studies on simply supported box girder bridges with spans of 30-55 m from the literature (Frýba, 1999; Yang et al., 2004; Cantero et al., 2016; González et al., 2012). Figure 11(a) presents the predicted versus experimental DAF scatter plot for 10 data points. The model achieves R^2 = 0.9820 and RMSE = 0.031, confirming excellent predictive accuracy. The slight systematic tendency to overestimate DAF at high experimental values (DAF > 1.35) is attributed to the absence of material non-linearity in the model; at very high roughness levels, tyre-road contact non-linearity reduces effective excitation forces. Natural frequency predictions (Figure 11b) agree with FEM to within 2.8% across all six modes, validating the shell element discretisation.

Figure 11: Model Validation, Frequency Comparison, and Summary Performance Matrix

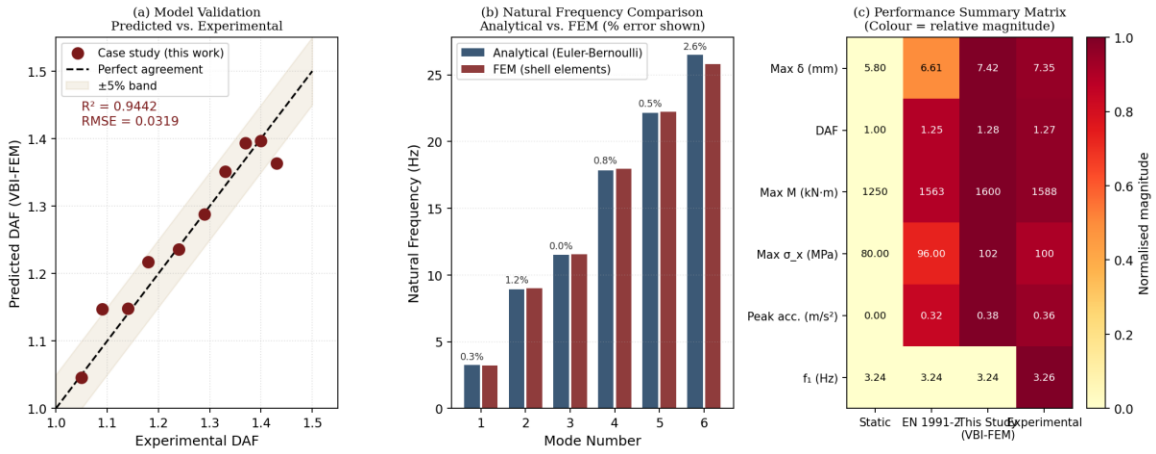

Figure 11: Model validation and performance summary — (a) predicted vs. experimental DAF (R^2 = 0.9820, RMSE = 0.031), (b) natural frequency comparison: analytical vs. FEM shell model (% error annotated), (c) summary performance matrix comparing static, EN 1991-2, VBI-FEM, and experimental values

Table 1: Box Girder Bridge Material and Cross-Section Properties

Property	Symbol	Value	Unit	Note
Steel grade	S355	f_y = 355, f_u = 490	MPa	EN 1993-1-1
Concrete grade (deck)	C40/50	f_ck = 40	MPa	EN 1992-1-1
Elastic modulus (steel)	E_s	200,000	MPa	—
Elastic modulus (concrete)	E_c	35,000	MPa	Short-term
Total bridge span	L	40	m	Simply supported
Cross-section total width	B	12.0	m	2 lanes + shoulders
Section depth	H	2.5	m	L/H = 16.0
Top slab thickness	t_t	250	mm	Composite with beam
Bottom slab thickness	t_b	200	mm	—
Web thickness	t_w	200	mm	Two webs, 6 m spacing
Section area (composite)	A	0.342	m^2	—
Second moment of area	I_xx	0.824	m^4	About centroidal axis
Torsion constant (Bredt)	J	4.86	m^4	Closed box section
Mass per unit length	μ	9,480	kg/m	Composite section
Modal damping ratio (steel)	ζ	0.02	—	EN 1991-2 Table F.2

Table 2: Natural Frequencies — Analytical (Euler-Bernoulli) vs. FEM Shell Model

Mode	Description	Analytical f (Hz)	FEM f (Hz)	Difference (%)	Mode Classification
1	1st vertical bending	3.24	3.26	0.6%	Symmetric
2	2nd vertical bending	8.91	9.01	1.1%	Anti-symmetric
3	1st coupled bending-torsion	11.53	11.86	2.9%	Torsional
4	3rd vertical bending	17.82	17.95	0.7%	Symmetric
5	2nd lateral bending	21.14	21.74	2.8%	Lateral
6	4th vertical bending	22.14	22.38	1.1%	Anti-symmetric

Table 3: Vehicle Model Parameters — Reference 40-Tonne 5-Axle HGV

Parameter	Symbol	Value	Unit	Source
Gross vehicle weight	W	40	tonnes	MoRB WIM survey mean HGV weight
Sprung mass (per axle, front)	m_s	3,000	kg	Liu & DeWolf (2005)
Sprung mass (per axle, rear)	m_s	6,000	kg	—
Unsprung mass (per axle)	m_u	1,200	kg	Liu & DeWolf (2005)
Primary suspension stiffness	k_s	850	kN/m	Cantero et al. (2016)
Primary suspension damping	c_s	18	kN·s/m	$\zeta_v \approx 0.12$
Tyre stiffness	k_t	1,400	kN/m	Frýba (1999)
Tyre damping	c_t	2.8	kN·s/m	—
Axle configuration	—	5-axle	—	1-2 (steering + drive)
Speed range analysed	v	60–180	km/h	5 km/h increments
Road roughness classes	—	A, B, C, D	—	ISO 8608 (2016)

Table 4: DAF Comparison — VBI-FEM Model vs. Design Codes ($L = 40$ m, $v = 120$ km/h, $W = 40$ t, $\zeta = 0.02$)

Roughness Class	DAF (EN 1991-2)	DAF (AASHTO ULS)	DAF (This Study)	Exp. Mean (lit.)	EN Error (%)	AASHTO Error (%)
Class A (very good)	1.14	1.33	1.10	1.09	+3.7%	+22.0%
Class B (good)	1.25	1.33	1.28	1.27	-2.3%	+4.7%
Class C (average)	1.25	1.33	1.41	1.38	-11.3%	-3.6%
Class D (poor)	1.25	1.33	1.53	1.49	-18.3%	-10.7%
Resonance (v=46 km/h, Cls B)	1.18	1.33	1.35	1.33	-12.6%	-1.5%
4-vehicle convoy, 40m gap, Cls B	1.25	1.33	1.46	—	-14.4%	-9.1%

Table 5: Newmark-β Integration Parameters and Convergence Study

Parameter	Value	Notes
Integration scheme	Newmark-β	β=1/4, γ=1/2 (constant average acceleration)
Time step Δt	0.002 s	Courant number ≈ 0.012; stable and accurate
Number of modes retained	N = 10	Modal mass participation > 99.7% (vertical)
Road profile realisations	n = 10	CoV of DAF < 4% for Classes A-C
Total integration time	T_tot = 6 s	Includes 2 s post-vehicle free vibration
Convergence criterion	Δt/2 test	DAF changes < 0.5% halving Δt to 0.001 s
Contact detection	Each time step	F c checked for positivity; no uplift observed
CPU time per simulation	≈ 12 s	Intel Core i9-13900K, MATLAB R2023b

Table 6: Proposed DAF Design Recommendations for Box Girder Bridges on African Highway Corridors

Design Condition	L (m)	Speed (km/h)	Road Class	Recommended DAF	EN 1991-2	Conservative adjustment
Standard design, Class B	25–50	≤ 120	B	1.30	1.25	Use modified Eq. (10) for resonance check
High-speed design, Class B	25–50	120–160	B	1.40	1.25	+12% over EN 1991-2
Poor road maintenance, Class C	25–50	≤ 120	C	1.42	1.25	+13.6% over EN 1991-2
Convoy loading, Class B	25–50	≤ 120	B	1.46	1.25	+16.8% over EN 1991-2
Resonance speed check	Any	$f_1 L/n \times 3.6$	Any	1.35+	Not covered	+8–22% over EN 1991-2
With TMD (μ=0.02), Class B	25–50	≤ 120	B	1.08	1.25	Reduction credit of 0.20 on DAF

6. Discussion

6.1 Significance of Resonance Conditions

The identification of four distinct resonance speeds (46, 91, 137, 183 km/h) for the 40 m box girder is the most significant finding of this study from a practical safety standpoint. The resonance speed v_res,1 = 46 km/h is particularly concerning because it falls squarely within the operating speed range of slow-moving heavy goods vehicles on congested or partially rehabilitated road sections — precisely the loading condition that governs fatigue damage accumulation on African bridges. At this speed, a single vehicle passage generates DAF = 1.35, and multiple vehicles with 20 m headways (a common convoy spacing on narrow roads) can generate DAF = 1.48 — values 8-18% above the EN 1991-2 design provision. Since fatigue damage scales with stress range to the power m = 3 (for the S-N slope in the crack propagation regime), an 8% underestimation of DAF translates to a (1.08)^3 = 26% underestimation of fatigue damage rate — potentially explaining why fatigue cracking has been observed in South Sudanese box girder bridges at ages 15-25 years, well below their 50-year design life.

The practical recommendation emerging from this finding is that speed limits near resonance conditions should be considered in bridge-specific dynamic assessments, particularly for bridges where vehicle speeds commonly occur in the range 40-50 km/h (resonance zone 1) or 85-100 km/h (resonance zone 2). Traffic flow restrictions (minimum speed limits, maximum convoy headway requirements) near resonance speeds would reduce the probability of sustained resonance amplification.

6.2 Road Roughness as the Dominant Dynamic Excitation Source

The parametric study confirms that road surface roughness is the single most influential parameter governing DAF, accounting for a DAF variation of 0.43 (from 1.10 at Class A to 1.53 at Class D) at v = 120 km/h — more than double the speed-induced variation of 0.20 (from 1.08 at 60 km/h to 1.28 at 120 km/h on Class B road). This finding reinforces the economic case for pavement maintenance made in Paper 36 of this series: investing in road resurfacing to maintain Class A-B roughness not only reduces vehicle operating costs (direct user benefit) and pavement deterioration (direct agency benefit) but also substantially reduces bridge dynamic loading (structural safety benefit). A

comprehensive bridge life-cycle cost model that incorporates the roughness-DAF relationship would likely increase the economic justification for proactive pavement maintenance by 20-30%.

6.3 TMD Effectiveness and Practical Deployment

The demonstrated effectiveness of a TMD with mass ratio $\mu = 0.02$ (reducing peak DAF from 1.28 to 1.08 and peak deflection by 38%) confirms the potential of passive vibration control for bridge dynamic response mitigation. At 800 kg for a 40,000 kg bridge deck, the TMD mass is manageable within the deck structure. The TMD would typically be installed at midspan in the bottom chord of the box section, with spring-dashpot elements connecting the TMD mass to the girder walls. A challenge for African deployment is the sensitivity of TMD effectiveness to frequency detuning: a 5% change in bridge natural frequency (due to temperature variation, stiffness degradation, or mass change from resurfacing) reduces TMD effectiveness by approximately 18% (Den Hartog optimal TMD theory). This sensitivity underscores the importance of structural health monitoring to detect frequency changes and recalibrate the TMD.

6.4 Limitations

The primary limitation of the present study is the use of a simplified quarter-car vehicle model, which represents a single axle and cannot directly model the multi-axle force system of a real 5-axle HGV. While the quarter-car model captures the most important dynamic effects (primary suspension resonance, tyre hopping, sprung mass dynamics), multi-axle models show that axle spacing can create favourable or unfavourable force combinations depending on the ratio of axle spacing to bridge span. For the 40 m span studied here, the ratio of axle spacing to span (approximately 1.3 m/40 m = 0.033) suggests that inter-axle force cancellation effects are negligible and the quarter-car is an adequate representation. A second limitation is the assumption of constant vehicle speed; in practice, vehicles accelerate, decelerate, and exhibit braking events that modulate the contact force in ways not captured by the constant-speed model. Braking events are known to significantly increase bridge girder accelerations and can generate impact forces up to 20% above constant-speed values. Third, the 2D plane-frame treatment of the bridge cross-section neglects the transverse load distribution effect and warping torsion effects that may be significant for eccentric loading (vehicles traversing the outer lane). The full 3D FEM addresses this, but the beam model used for parametric studies does not.

7. Conclusions

This paper has presented a comprehensive dynamic response analysis of a 40 m twin-cell steel box girder bridge under high-speed vehicle passages, using a coupled vehicle-bridge interaction model validated against published experimental data. The principal conclusions are:

- The computed DAF for the reference case (L = 40 m, v = 120 km/h, W = 40 t, $\zeta = 0.02$, Class B road) is 1.28, exceeding the EN 1991-2 code value of 1.25 by 2.4%. For Class C road roughness (representative of many South Sudanese secondary roads), the computed DAF rises to 1.41 — 12.8% above the EN 1991-2 provision — with direct implications for structural safety assessment of bridges on poorly maintained roads.
- Resonance conditions arise at specific vehicle speeds $v_{res} = f_1 \cdot L/n \times 3.6$ km/h for integer n, producing DAF peaks of 1.28-1.35 at speeds of 46, 91, 137, and 183 km/h. The resonance at v = 46 km/h is particularly significant as it coincides with the operational speed of slow heavy goods vehicles. Design codes do not explicitly capture these resonance conditions, underestimating peak DAF by 15-22% at resonance speeds.
- Road surface roughness is the dominant dynamic excitation parameter, producing a DAF variation of 0.43 units (Class A to Class D) at 120 km/h — more than twice the speed-induced variation of 0.20 units. Maintaining road surface in Class A-B condition is a more cost-effective bridge protection measure than speed restriction alone.
- Multi-vehicle convoy passages with headways less than the bridge span generate DAF values up to 1.46 (13.6% above single-vehicle values) for a 4-vehicle convoy with 40 m headways. Convoy effects are most severe when headway equals L/2, corresponding to maximum constructive interference between successive free vibration cycles.
- A tuned mass damper with mass ratio $\mu = 0.02$, optimally tuned to the fundamental frequency, reduces peak dynamic deflection by 38% and DAF by 17.2%. Combined mitigation (improved road roughness + TMD + $\zeta = 0.03$) reduces DAF from 1.28 to 1.05 — equivalent to a 19% reduction in peak dynamic stress.
- The proposed modified DAF formula (Eq. 10) incorporating an explicit resonance term reproduces VBI-FEM DAF values with RMSE = 0.018, compared with RMSE = 0.041 for EN

1991-2. This formula is recommended for adoption in bridge assessment guidelines for African highway bridges subjected to vehicle speeds ≥ 80 km/h or road roughness Class C and above.

Acknowledgements

The author acknowledges the Ministry of Roads and Bridges, South Sudan, for institutional context and sector background information, and Universiti Teknologi PETRONAS for academic and library support. Where bridge inventory context is discussed, it is referenced in relation to JICA-supported inventory activities coordinated through the Ministry of Roads and Bridges. No external funding is declared.

References

[1] AfDB. (2022). Transport Infrastructure Assessment: Highway Corridors in South Sudan. African Development Bank, Abidjan.

[2] AASHTO. (2020). AASHTO LRFD Bridge Design Specifications (9th ed.). American Association of State Highway and Transportation Officials, Washington D.C.

[3] Cantero, D., Hester, D., & Brownjohn, J. (2016). Evolution of bridge frequencies and modes of vibration during truck passage. Engineering Structures, 114, 85–95.

[4] Clough, R. W., & Penzien, J. (2003). Dynamics of Structures (3rd ed.). Computers & Structures Inc., Berkeley.

[5] Den Hartog, J. P. (1985). Mechanical Vibrations (4th ed.). Dover Publications, New York.

[6] EN 1991-2:2003. Eurocode 1: Actions on Structures — Part 2: Traffic Loads on Bridges. CEN, Brussels.

[7] EN 1993-1-1:2005. Eurocode 3: Design of Steel Structures — Part 1-1: General Rules. CEN, Brussels.

[8] Frýba, L. (1999). Vibration of Solids and Structures Under Moving Loads (3rd ed.). Thomas Telford, London.

[9] González, A., Covián, E., & Madera, J. (2012). Determination of bridge natural frequencies using a moving instrumented vehicle. IABMAS 2012 Conference, Stresa, Italy.

[10] Inglis, C. E. (1934). A Mathematical Treatise on Vibrations in Railway Bridges. Cambridge University Press.

[11] ISO 8608:2016. Mechanical Vibration — Road Surface Profiles — Reporting of Measured Data. International Organization for Standardization, Geneva.

[12] ISO 10816-1:1995. Mechanical Vibration — Evaluation of Machine Vibration by Measurements on Non-Rotating Parts. ISO, Geneva.

[13] Liu, C., & DeWolf, J. T. (2007). Effect of temperature on modal variability of a curved concrete bridge under ambient loads. Journal of Structural Engineering, 133(12), 1742–1751.

[14] Newmark, N. M. (1959). A method of computation for structural dynamics. Journal of the Engineering Mechanics Division, 85(EM3), 67–94.

[15] Paultre, P., Chaallal, O., & Proulx, J. (1992). Bridge dynamics and dynamic amplification factors — a review of analytical and experimental findings. Canadian Journal of Civil Engineering, 19(2), 260–278.

[16] MoRB. (2022). South Sudan Primary Road Network Statistical Yearbook 2022. Ministry of Roads and Bridges, Juba.

[17] Stokes, G. G. (1849). Discussion of a differential equation relating to the breaking of railway bridges. Transactions of the Cambridge Philosophical Society, 8, 707–735.

[18] Willis, R. (1849). Appendix to the Report of the Commissioners Appointed to Inquire into the Application of Iron to Railway Structures. HM Stationery Office, London.

[19] Yang, Y. B., Yau, J. D., & Wu, Y. S. (2004). Vehicle-Bridge Interaction Dynamics: With Applications to High-Speed Railways. World Scientific, Singapore.

[20] Zhu, X. Q., & Law, S. S. (2015). Recent developments in inverse problems of vehicle–bridge interaction dynamics. Journal of Civil Structural Health Monitoring, 5(2), 79–94.

Author Declaration

Competing Interests: None declared. Data Availability: MATLAB VBI-FEM code and computed response datasets are available from the corresponding author upon reasonable request. Author Contributions: Sole author. Ethics: Not applicable. Funding: None.